Desalination 593 (2025) 118237

Contents lists available at ScienceDirect

Desalination

journal homepage: www.elsevier.com/locate/desal

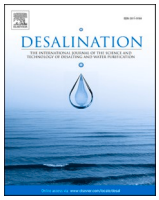

Perylene diimide-derived supramolecules-modified graphene sponge as a high-efficiency solar steam generator

Elif Erçarıkcı [a], Demet Demirci Gültekin [b], Ezgi Topçu [a], Züleyha Kudaş [a], Murat Alanyalıoğlu [c], Kader Dağcı Kıranşan [a,*]

[a] Department of Chemistry, Science Faculty, Atatürk University, Erzurum 25240, Türkiye
[b] Department of Chemical Technology, Vocational School of Technical Science, Atatürk University, Erzurum 25240, Türkiye
[c] Bilecik Şeyh Edebali University, Vocational School, Department of Food Processing, Bilecik 11100, Türkiye

HIGHLIGHTS

- Preparation of a novel freestanding perylene diimide-derived supramolecules (PDI) modified three-dimensional (3D) gradient hydrophobic GrS (PDI/GGrS).
- PDI allowed us to achieve perfect absorption of broad-band sunlight and GGrS facilitated water transport through channels of sponge structure.
- A high rate of sunlight absorption and photothermal conversion, due to the gradient structure of GGSM and PDI.
- This study can provide new possibilities for harvesting solar energy by producing clean water from seawater, wastewater, and even acidic/alkali solutions

ARTICLE INFO

Keywords:
Graphene sponge
Gradient structure
Solar energy
Clean water
Perylene diimide

ABSTRACT

Generating steam using solar energy appears to be an effective approach to obtaining clean water, especially from salty water and wastewater, since the sun is a natural and constant source. Compared to many methods, studies in solar steam generation have accelerated due to being highly efficient, sustainable, and low-cost. Graphene sponges (GrSs), possessing structural flexibility and effective photothermal activity, are widely used for this purpose. However, the hydrophobic character of these materials limits their effectiveness in solar steam generators. At this point, we prepared perylene diimide-derived supramolecules (PDI) modified three-dimensional (3D) gradient hydrophobic GrS (PDI/GGrS) as the highly efficient solar thermal converter for the generation of clean water. PDI allowed us to achieve perfect absorption of broad-band sunlight and GGrS facilitated water transport through channels of sponge structure. As a result, PDI/GGrS has achieved a high water evaporation rate of 3.5 kg h^{-1} m^{-2} with a superior solar thermal conversion efficiency of up to 90 %. This study can provide new possibilities for harvesting solar energy by producing clean water from seawater, wastewater, and even acidic/alkali solutions.

1. Introduction

Due to the increasing population worldwide, scarcity of clean water has become one of the most urgent problems in human life [1–6]. To find a solution to this problem, great efforts have been made in the utilization of solar irradiation as a renewable and sustainable energy source [7–10]. Solar steam generators, a potential technology to absorb solar energy and generate heat at the water-air interface, have attracted great attention in desalinating seawater and purifying heavy metals and dyes from water [11–14]. Therefore, there is a significant need to develop materials that have high solar thermal conversion, evaporation rates, and broadband light absorption for steam generation. An ideal solar steam generation system should not only have outstanding light absorption but also excellent photothermal conversion, and a high rate of clean water production as well as stability in extreme conditions (in strong acid and alkali solutions) [15–18]. Meanwhile, Janus structured materials possessing two different parts, such as hydrophobic-hydrophilic properties have been investigated for steam generation [19].

As a part of the research on the conversion of sunlight into thermal

* Corresponding author.
E-mail address: kdagci@atauni.edu.tr (K. Dağcı Kıranşan).

https://doi.org/10.1016/j.desal.2024.118237
Received 16 July 2024; Received in revised form 21 October 2024; Accepted 21 October 2024
Available online 22 October 2024

energy, various studies have been conducted over the last few decades. Examples of these materials include vertically aligned graphene sheet membranes [18], double-sided reduced graphene oxide films [20], polydopamine and silver nanoparticles deposited wood [21], poly-(ethylene glycol) diacrylate and polyaniline hydrogel [22], MoS_2-cotton cloth [23], and Au − CuS gyroid-structured materials [24]. Janus structures prepared by applying Aluminum phosphorus [25] and Ag-polydopamine [21] composite on natural wood achieved evaporation rates of 1.48 and 1.53 kg/m^2h and 90 % and 88 % solar conversion efficiency, respectively. Similarly, Yin et al. reported that the photothermal material prepared by modifying cellulose foam with polyethyleneglycol-polyaniline composite has an evaporation rate of 1.40 kg/m^2h and a thermal efficiency of 91 % [22]. Chen et al. prepared photothermal material with polypyrrole on melamine foam which achieved an evaporation rate of 2 kg/m^2h and a solar conversion efficiency of 91 % [26]. The disadvantage of Janus materials is that the preparation procedure for most of them is costly and time-consuming. Unlike Janus structure materials, the utility of single materials, that both adsorb sunlight and can transport high amounts of water, has been investigated in the solar steam generator system. For example, only a three-dimensional fiber aerogel was prepared by Tang et al., it achieved an evaporation rate of 1.43 kg/m^2h, and a thermal efficiency of 85 % when this material was used directly in the solar steam generator system [27]. Similarly, Yang et al. studied solar steam generation with 3D graphene [28], whereas Qu et al. with vertically aligned graphene sheets membrane [18]. These studies have shown that single materials possess relatively low efficiency of solar thermal conversion. Hereof, efforts to develop new materials with high steam generation efficiency that can be prepared practically continue unabated.

Graphene, a one-atom-thick and two-dimensional packed honeycomb lattice, has distinguished itself among its peers owing to not only its high photothermal efficiency and light absorption but also its excellent electrical and thermal conductivity, and superior mechanical strength [29]. Graphene oxide (GO), which is chemically exfoliated from graphite, is frequently used for the fabrication of free-standing and well-ordered hydrogel-based 3D materials [30,31]. However, one limiting factor of graphene-hydrogel-based solar evaporators is the hydrophobic character of this material. Graphene hydrogel (sponge) can convert sunlight into heat energy at a high rate as a photothermal material in the solar steam generator system [8,19]. Nevertheless, since it is quite hydrophobic, it cannot transport water adequately, resulting in low thermal efficiency [10,32]. In our previous study [33], a graphene sponge with a gradient structure was prepared, in which the hydrophobic properties gradually decreased from one end to the other. This gradient graphene material achieved higher thermal conversion and evaporation performance, compared to pure graphene sponge [33].

Supramolecules are a collection of chemicals consisting of different molecules that have been in the field of chemistry for many years, although supramolecules stand out with their structural and functional properties [34]. Compared to traditional organic substances, supramolecules provide light absorption at a wide wavelength due to their flexible and numerous π conjugated systems.

The photophysical or photochemical process of a supramolecule is initiated by the absorption of light, leading to an electronically excited state. The excited state is unstable due to excess energy and prefers one of the molecular processes either radiative emission (fluorescence or phosphorescence relaxation), vibrational relaxation (heat), or intersystem transfer. Among these processes, any non-radiative process leads to the conversion of light energy into heat energy [34]. Since all these processes are competitive, photothermal conversion efficiency increases especially if fluorescence, intersystem transfer, and photochemical reactions are inhibited [35]. To increase the photothermal efficiency of supramolecules, their fluorescence efficiency can be reduced by adsorbing them on a solid support material. Thus, the supramolecules, which exhibit high fluorescence activity in a solution and a free state, this property decreases by 80 % when adsorbed to the surfaces of solid materials such as graphene oxide (GO) [36] and boron nitride (via π-π interactions or electrostatic interactions) [37]. Since there is no electron transfer after adsorption in this way, the absorbed energy is mostly reflected as photothermal energy. Perylene diimide derivatives (PDIs) are the leading supramolecules whose photothermal properties are investigated. PDIs form numerous absorption bands in both the near-IR and UV–visible regions [37,38]. Photothermal transformations of these molecules are examined in various fields such as catalysis, micromotors and actuators, especially in biomedical applications. For instance, Zhang et al. reported that a PDI-derived supramolecule absorbs light energy at a high rate even in the near-IR region in the radical state, and converts it into thermal energy [39].

In our previous study, we developed a gradient-structured 3D graphene sponge, which has a 3D network of graphene sheets with a highly porous structure, lightweight, and gradually hydrophobic character [33]. Because of the excellent absorption of water with the gradient hydrophilic-hydrophobic property of this material, we believe that such a gradient-graphene sponge (GGrS) would be an ideal surface for the modification of PDI molecules. Herein, we report GGrS modified with PDI, which can absorb high amounts of sunlight in both UV–vis and IR regions for steam generation. This gradient material was obtained by immersing a part of 3D GrS in the PDI solution. PDI/GGrS is used as photothermal material in solar steam generators. The wide wavelength sunlight absorption and high photothermal conversion of graphene and PDI, this material exhibited steam generation about 3 times performance compared to GGrS.

2. Experimental section

2.1. Preparation of GGrS

GO dispersion was prepared from graphite powder using a modified Hummers method, as reported previously [40]. First, the graphene sponge (GrS) was fabricated using the freezing-air drying technique. Briefly, 20 mL of GO aqueous dispersion containing ascorbic acid (AA, 400 mg) as a reductant was vigorously stirred after the addition of sodium dodecyl sulfate (SDS) (50 % by weight) for foaming. The resulting foamy dispersion was treated at 75 °C for 1 h and the graphene hydrogel sponge (GHS) was obtained. GHS was frozen at −18 °C for about 5 h and then cooled naturally to room temperature. Subsequently, the as-prepared GHS was dried at 90 °C, then washed several times with ethanol and deionized water to remove excess AA. Finally, free-standing GrS was fabricated by annealing GHS at 350 °C. Fig. S1 shows XRD patterns of GHS and GrS. The XRD data of GHS exhibits both the peaks corresponding to (001) plain of GO at 10.9° and (002) diffraction of rGO at 22.4°. On the other hand, in the XRD pattern of GrS, the diffraction peak of GO completely disappeared and the (002) crystal peak of rGO, which is dominant in the chemical structure, was observed. These results indicate that the reduction with AA is not sufficient, and annealing at 350 °C is necessary to obtain a more water-resistant material.

Then GGrS was prepared with a simple acid impregnation, as in our previous study [33]. To convert GrS to GGrS, GrS with about a height of 12 mm and a diameter of 10 mm was prepared and only 0–4 mm of it was immersed in the 10 mL acid solution containing $H_2SO_4/HNO_3 = 1$ for 5 min. GGrS was obtained after washing with pure water and drying in the air. GGrS, which has a thickness of about 12 mm, was divided into 3 different parts depending on the different oxidations of the graphene structures, as illustrated in Fig. 1.a. The part between 0 and 4 mm (P1) directly treated with acid is the most oxidized, the part between 4 and 8 mm is partially oxidized (P2), and finally the part between 8 and 12 mm possesses a hydrophobic structure (P3) [33].

2.2. Synthesis of PDI

PDIdS, Perylene diimide derivatives, were synthesized and this molecule was analyzed with NMR and Maldi-TOF. The experimental

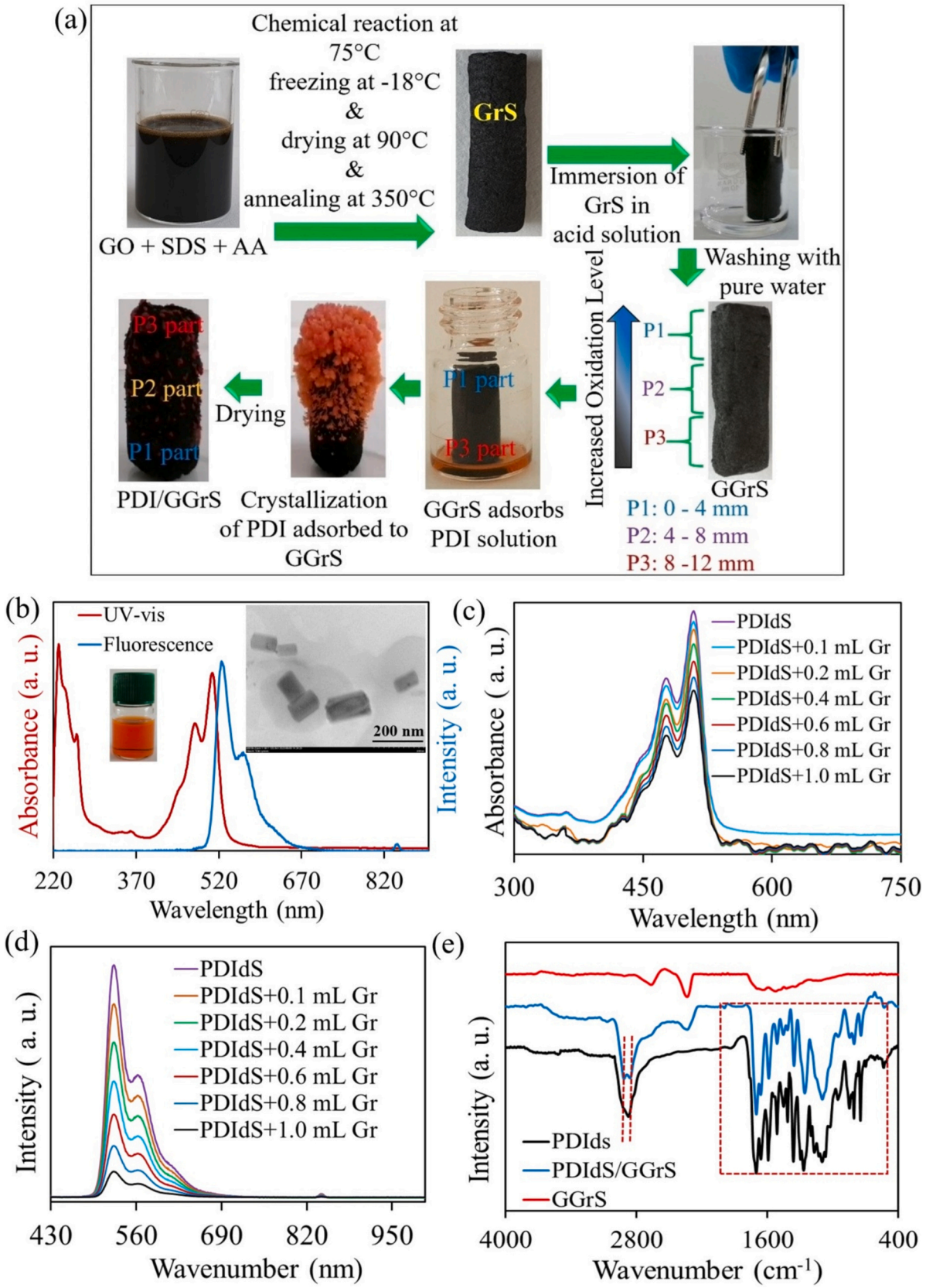

Fig. 1. (a) Preparation procedure of PDI/GGrS. (b) UV–visible absorption and fluorescence spectrum of PDI. Inset: TEM image of PDI. UV–visible absorption (c) and fluorescence spectra (d) of the solution obtained by adding different volumes of rGO dispersion to PDI. (e) FTIR spectra of PDI, PDI /GGrS, and GGrS.

steps, NMR (Fig. S2), Maldi-Tof mass (Fig. S3) spectra, and chemical structure of the resulting product (Fig. S4) were presented in detail in Supporting Information. Briefly, Perylene diimide tetracarboxylic dianhydride (PTCDA) (2.1 g, 5.35 mmol), 1,8-Diazabicyclo[5.4.0]undec-7-ene (DBU) (3.1 g, 20 mmol) and tri ethylene glycol mono methyl ether (6.7 g, 40 mmol) were dissolved in 10 mL DMF. After adding teg-tosyl (13 g, 40 mmol) dissolved in 10 mL DMF to the mixture, the reaction was carried out at 60 °C.

After the reaction, red solid perylene tetra carboxylic tetraester (PTTE) was obtained. PTTE (4.6 g, 4.6 mmol) and p-toluene sulfonic acid monohydrate (900 mg, 4.6 mmol) were mixed in 10 mL of toluene at 95 °C for 5 h. Then the temperature was reduced to 75 °C and 15 mL of THF was added to the solution. After stirring at 75 °C for 1 h, 200 mL of methanol was added to the mixture which was cooled to room temperature. A red PTTE-anhydride product was obtained after the filtration process. PTTE-anhydride (500 mg, 0.71 mmol), *p*-phenylene diamine (38 mg, 0.35 mmol) and 40 mg Zn(OAc).H_2O in 10 mL DMF were mixed at 120 °C for 2 days to obtain dark red solid perylene monoanhydride diester (PMADE).

2.3. Preparation of PDI/GGrS

For the modification of PDI to GGrS, a 0.5 mg/mL solution of PDI in dichloromethane (DCM) was prepared, and the GrS was immersed from P3 side in this solution (2 mm in height in the container). Thus, the 5 mg PDI was adsorbed to GGrS. Parameters such as the concentration of PDI and the immobilization time of GGrS were optimized. Cylindrical sponges with a height of 12 mm and a diameter of 10 mm were used in the optimization studies for obtaining GGrS from GrS and for PDI immobilization on GGrS. Disk-like sponges with a height of 12 mm and a diameter of 50 mm were employed in solar steam generator applications. The experimental procedure for preparing PDI/GGrS and the video of the drying of PDIdS after adsorption to GGrS are presented in Fig. 1.a and Video S1, respectively.

2.4. Characterization

Fourier transform infrared (FTIR) spectroscopy was performed for the structural analysis of the samples using a PerkinElmer spectrometer. The morphology and structure of PDI/GGrS were investigated by field emission scanning electron microscopy (FESEM, ZEISS SIGMA 300) equipped with an energy-dispersive X-ray spectroscopy (EDX). Optical characterizations of PDI was analyzed by using a UV–vis-NIR spectrophotometer (Shimadzu 3101PC). The microstructure of PDI was investigated by transmission electron microscope (TEM, Hitachi HT7700). The crystal structure of the samples was analyzed by X-ray powder diffraction (XRD) using a Rigaku Mini Flex X-ray diffractometer with Cu Kα radiation (λ = 1.5406 Å). Agilent Cary Eclipse Brand Fluorescence was used to examine the fluorescence properties of PDI. Raman spectra of the samples were attained from a Raman microscope (WITech alpha 300R) at an excitation laser wavelength of 532 nm. The atomic ratios of elements in PDI/GGrS were characterized using the X-ray photoelectron spectroscopy (XPS, Spect-Flex spectrometer), equipped with a monochromatic Al Kα X-ray source.

2.5. Steam generation experiments

Solar steam generation experiments were acquired in a system shown in Fig. 4.a. The floated PDI/GGrS on the water surface was used as a direct photothermal material. Both surface temperatures and the weight loss over the entire process were recorded using an IR camera and electronic mass balance, respectively. The samples were irradiated by a solar simulator from 1 (1 kW m^{-2}) to 10 sunlight (10 kW m^{-2}). 10 sunlight was used in the desalination and purification studies with PDI/GGrS. All experiments were carried out at room temperature. The surface temperature of GGrS and PDI/GGrS were determined during desalination experiments. PDI/GGrS employed in solar steam generation costs about €0.3.

2.6. Antibacterial test

E. coli cells were grown in Luria Broth (LB) medium for 12 h at 37 °C. Before the antibacterial test, *E. coli* cells were harvested at the exponential growth phase by centrifugation at 6000 rpm for 3 min. PDI/GGrS was first soaked in 75 % alcohol for 30 min and then washed with phosphate buffer solution. After adding 5 mL of *E. coli* suspension (10^6 CFU/mL) onto PDI/GGrS in a sterilized Petri dish, the whole sample was placed in an incubator shaker. The colony counting assay method was applied at regular intervals for 24 h to determine the amount of *E. coli* bacteria changes.

3. Result and discussion

3.1. Photochemical and Morphological Properties of PDI

The absorption properties of the synthesized PDI were characterized using UV–visible absorption spectroscopy. PDI contain high-intensity absorption bands at the visible and UV regions between 680 and 220 nm, as shown in Fig. 1.b. The peaks between 520 and 370 nm correspond to the quantum vibration properties of υ = 0 → υ' = 0, 1, 2, 3 excitation states. Here, υ and υ' are the quantum vibration numbers of the ground and excited states, respectively. In this context, the peaks that occurred at 510 and 479 nm correspond to 0 → 0 and 0 → 1, and the shoulder peak at 445 nm corresponds to 0 → 2 quantum vibrational peaks [41]. Such different quantum vibrational states arise from π-π* electronic transitions with different electronic properties found in the PDI-derived supramolecule [42]. The emission peaks at 568, 567, and 621 nm in the fluorescence spectrum of PDI are mirror images of the quantum vibration peaks occurring in the UV–visible absorption spectrum (Fig. 1.b) [42]. The peaks at 510, 479 and 44 nm in the UV–visible absorption spectrum were red-shifted to 18, 88, and 177 nm in the fluorescence spectrum, respectively, due to the Stokes shift. As expected, the fluorescence of supramolecules is quite high and is compatible with their absorption properties. Increasing volumes of rGO dispersion were added to the PDI solution and UV–visible and fluorescence spectra of the prepared mixtures were recorded in Fig. 1.c and d, respectively. Due to the adsorption of PDI to the surface of graphene layers through π-π interactions, there was a decrease in the absorption and fluorescence intensity of 25 % and 92 %, respectively. The lower decrease in absorption is attributed to the fact that PDI can relax with thermal transformation, instead of fluorescence [39]. The morphological structure of PDI was investigated using TEM. The TEM image in the inset of Fig. 1.b showed that PDI has a regular and uniform rectangular prism-like crystal structure with a size of 180 nm.

3.2. Optimum parameters for preparation of PDI/GGrS

The structural properties of GGrS were investigated and presented in detail in our previous study [33]. FTIR spectroscopy was used to test whether PDI was immobilized onto the GGrS surface. The broad peak in the spectrum of GGrS in the 3000–3600 cm^{-1} range in Fig. 1.e corresponds to the O—H vibration. The peaks in the spectrum belong to the C—H vibration of the aromatic structure CO (at 2967 cm^{-1}), COOH (at 1733 cm^{-1}), and C–O–C (at 1624 cm^{-1}) vibrations of functional groups [43]. In the FTIR spectrum of PDI, peaks corresponding to aromatic C—H at 3124 cm^{-1}, aliphatic C—H at 2927 and 2874 cm^{-1}, and C═O stretching occurred at 1703 cm^{-1} and 1660 cm^{-1}. Additionally, peaks corresponding to conjugated C═C, C—N, and CH_2-O stretching are observed at 1593, 1363, and 1173 cm^{-1}, respectively, and peaks for C—H bending are formed at 810 and 743 cm^{-1} [44]. The presence of peaks of both PDI and GGrS in the FTIR spectrum of PDI/GGrS confirms that GGrS has been successfully modified with PDI. PDI was adsorbed to

the GGrS surface by π-π interactions due to the π conjugated systems in the structure of GGrS and supramolecules [36]. In addition, the peaks at 2855 and 2920 cm^{-1} in the FTIR spectrum of both GGrS and PDI/GGrS correspond to the symmetric and asymmetric vibrations of the C—H bond in the structure of rGO [45]. FTIR was used to optimize the solution concentration and immobilization time for the gradient modification of the GGrS with PDI (Fig. S5.a-d). When the concentration of PDI solution was lower than 0.5 mg/mL, vibration peaks of PDI were not observed for P3 in the FTIR spectrum of PDI/GGrS (Fig. S5.a). Additionally, when the immobilization time was less than 2 min, vibration peaks of PDI occurred only in P3, while no peak was detected in P2 (Fig. S5.b). After 2 min of immobilization (Fig. S5.d), intensive peaks were formed in P3 and partially in P2, indicating that PDI was gradually immobilized to GGrS (Fig. S5). The studies demonstrated that the optimum concentration and time were 0.5 mg/mL and 2 min, respectively.

3.3. Morphological and structural characterization of PDI/GGrS

In Fig. 2.a-c, the morphological structure of PDI/GGrS prepared under optimum conditions was examined using the FESEM. The presence of PDI with a rectangular prism-like crystal structure especially on the P3 part within the porous GGrS structure was observed in Fig. 2.a. PDIs, which are quite dense in the P3 part of PDI/GGrS, are partially observed in the P2 (Fig. 2.b) and are not seen at all in the P1 (Fig. 2.c), confirming the gradient structure of PDI/GGrS. In Fig. 2.d, the EDX spectrum of the P3 part of PDI/GGrS showed the presence of C, O, and N atoms in the structure in which C and O atoms originate from both the GrS structure and the supramolecule, the N atom is from PDI. The atomic ratio of three different parts of PDI/GGrS displayed that compared to P3, the presence of N decreased in P2 and became zero in P1 (inset of Fig. 2. d).

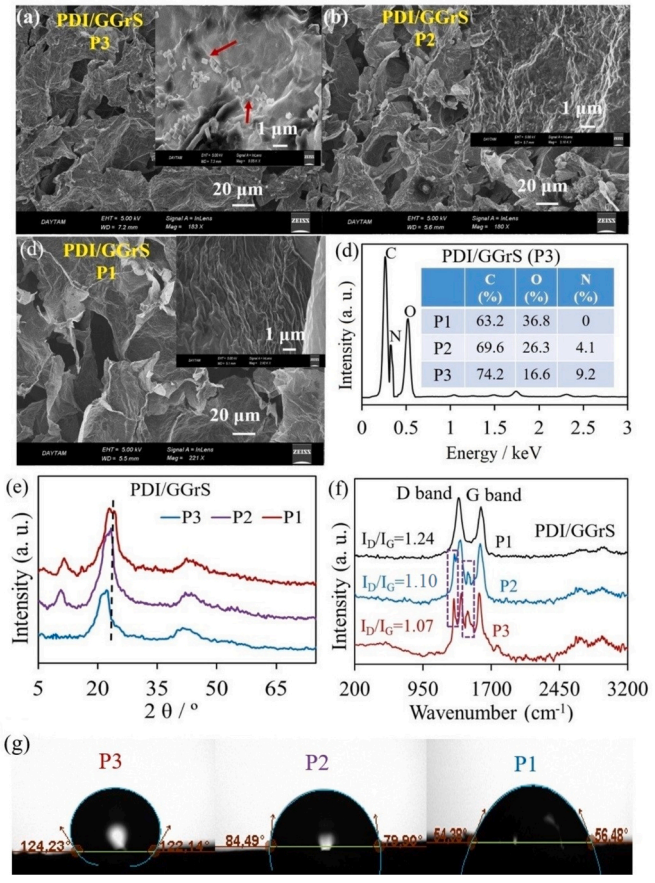

Fig. 2. FESEM images at low and high (in the inset of Figures) magnifications for (a) P3, (b) P2, and (c) P1 part of PDI/GGrS. (d) EDX spectrum of the P3 of PDI/GGrS. Inset: % atomic ratios of P3, P2, and P1 of PDI/GGrS. XRD (e) and Raman (f) spectra and water angle measurements (g) of P1, P2, and P3 of PDI/GGrS.

The XRD spectrum of PDI/GGrS in Fig. 2.e exhibited the characteristic graphene (002) and (100) diffraction peaks at 24.6° and 42.5°, respectively. The diffraction peaks at about 10.2° in P1 and P2 originated from the gradient hydrophilic structure of GGrS. These peaks correspond to the (002) diffraction of GO formed during oxidation with acid treatment in GGrS preparation [33]. On the other hand, the diffraction peaks of graphene shifted to lower 2θ values due to the oxidation effect which shows that adsorption of PDI preferentially occurs between rGO layers [46].

Fig. 2.f displays the Raman analysis of different parts of PDI/GGrS. Raman spectrum shows two typical peaks, centered at about 1360 and 1597 cm^{-1}, corresponding to the D-band (representing the defects due to the reduction of graphene sheets) and the G-band (corresponding to the vibrations of sp^2 C = C atoms in a 2-D hexagonal lattice), respectively. For P3 and P2, in addition to these bands, various peaks were formed due to the structure of PDIsS, corresponding to the C—C stretching for the plane of A_g mode (at 1292 cm^{-1}) and the C-C-H bending of B 3_g symmetry (at 1450 cm^{-1}) [47–49]. The absence of these additional peaks for P1 reveals that PDI has been gradually adsorbed to the GGrS. I_D/I_G ratios of P3, P2, and P1 of PDI/GGrS were determined as 1.07, 1.1, and 1.24, respectively. Thus, it was revealed that the gradient oxidative structure resulting from GGrS was preserved after PDI modification.

The water contact angle measurements of three parts (P3, P2, P1) of PDI/GGrS were presented in Fig. 2.g. A water contact angle of 124° was measured in the P3, indicating hydrophobic character of this part. It is also seen in Fig. 2.g contact angle decreases gradually for P2 and P1, confirming that gradient oxidation has been successfully performed on GrS. From these results, it was predicted that PDI/GGrS as a photothermal material in SSG application would be very effective in transporting water to the upper parts, especially with its gradient structure.

Fig. 3.a shows the XPS spectra of three parts of PDI/GGrS. While only C and O atoms originating from the GGrS structure was observed for P1, an N peak occurred due to PDI in addition to C and O atoms for P2 and P3. This is confirmed by the atomic ratios of three different parts of PDI/GGrS in Table S1. As the hydrophilic character in the structure increased (from P3 to P1), the atomic ratio of O increased, C decreased, and towards the hydrophobic part (from P1 to P3), the atomic ratio of N increased (Table S1).

Deconvoluted C 1s spectrumof P3 displayed the peaks corresponding to C-C/C=C (at 283.5 eV), C-OH (at 285.5 eV), and C—N (at 286.7 eV) bindings (Fig. 3.b). O 1s region has also exhibited C—O (at 531.3 eV), C-OH (at 533.1 eV), and C-O-C (at 535.4 eV) binding peaks (Fig. 3.c). For N 1s, peaks corresponding to N—C, N=C and N-C=O binding were observed at 397.5, 401.8, and 406.1 eV, respectively, attributed to that PDI is densely doped into the GGrS structure (Fig. 3.d) [50].

3.4. The water absorption of PDIdS/GGrS

One of the main parameters affecting the high performance of solar steam generators is the fast and effective absorption of water through the material. To test these parameters, PDI/GGrS (2 cm in height and 0.6 cm in diameter) were immersed in aqueous 4.0 mM Rhodamine B (Rh B) solution from the P1. The Rh B solution monitored by the camera reached the end point of PDI/GGrS in 45 s (Video S2). The slower water transport of PDI/GGrS than GGrS (10 s) [33] is attributed to the hydrophobic character of the supramolecules adsorbed to the structure. The weight (η_w,%) and volume (η_V,%) swelling ratio of PDI/GGrS measured at different temperatures were determined by Eq. S1 and Eq. S2, respectively, and the obtained results were presented in Table S2 [22]. As a result of the experiments, the water absorption rate of PDI/GGdS was calculated as 46.12 kg m^{-3} s^{-1}. The fact that the water

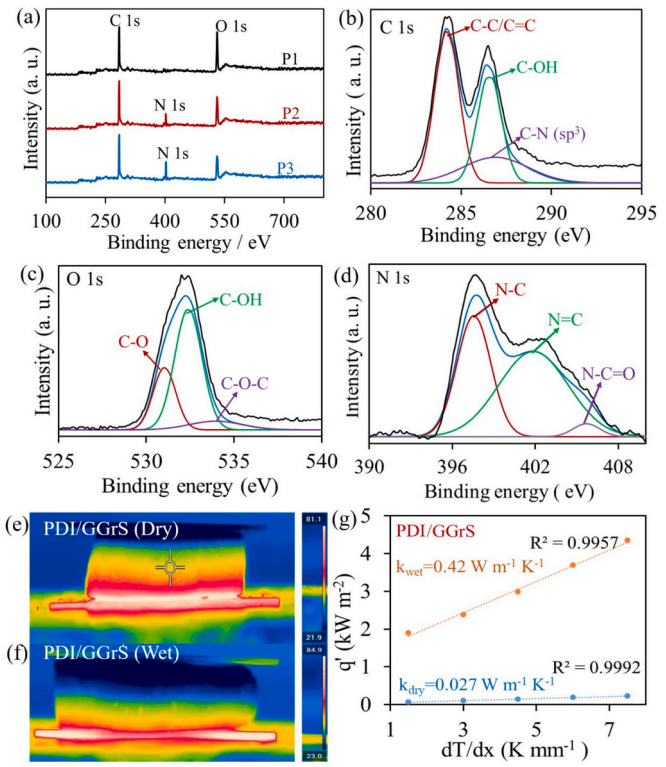

Fig. 3. (a) XPS spectrum of P1, P2, and P3 of PDI/GGrS. Deconvolution results C 1s (b), O 1s, (c) and N 1s (d) regions. Thermal camera images of (e) dry and (f) wet PDI/GGrS. (g) The thermal conductivity of PDI/GGrS.

transport and water absorption ratio of PDI/GGrS is lower than that of GGrS (61.72 kg m^{-3} s^{-1}) is attributed to the hydrophobic character of PDI in the material structure. The water absorption capacity of PDI/GGrS is higher than the steam production rate under 1 sunlight. Rapid water absorption is of great importance for the continuity of the process, as it prevents drying during steam production.

PDI/GGrS, which has a high water absorption property, can float on the water surface for a long time and even remain floating without any structural deformation at the end of the 7th day (Fig. S6).

3.5. Thermal conductivity of PDI/GGrS

The thermal conductivity of PDI/GGrS was determined with Eq. S3, as explained in detail in the Supporting Information. Since thermal insulation plays an important role in trapping heat on the evaporation surface during photothermal conversion, the thermal conductivity of both wet and dry PDI/GGrS was investigated in Fig. 3.e and f, and the results were presented in Table S3. [9,51]. PDI/GGrS exhibited a thermal conductivity much lower than that of water (0.61 W m^{-1} K^{-1}), which can be attributed to that this photothermal material acts as an effective thermal barrier to retain heat on the evaporating surface for solar steam generation.

3.6. Photothermal performance of PDI/GGrS

PDI/GGrS was investigated as photothermal material in solar steam generator applications at the experimental setup shown in Fig. 4.a. The digital photograph of PDI/GGrS and its image under UV light in the inset of Fig. 4.a demonstrated the gradient adsorption and surface modification of PDI, respectively. The evaporation rate of PDI/GGrS after 1 h is calculated as 3.50 kg/m^2 h, which is much higher than GGrS (1.79 kg/m^2 h) (Fig. 4.b) [33]. Such about 2-fold increase in evaporation rate is due to the high light absorption of supramolecules and their ability to convert the absorbed energy into thermal energy. In addition, the high photothermal efficiency of PDI can be attributed to the easy delocalization of electrons due to the regular conjugated system in its structure [38,52].

Fig. 4.c displays the surface temperature of water in the presence and absence of PDI/GGrS during 100 s irradiation time. The surface temperature of water increased from 20 °C to 23 °C, on the other hand, that of PDI/GGrS exceeded 70 °C. In Fig. 4.c, the photograph of the PDI/GGrS at the 40th second under sunlight and the vapor intensity can be seen generated by the material (Video S3). In Fig. 4.d, the time to reach the maximum temperature (72 °C) is only 50 s for PDI/GGrS, which indicates the high photothermal efficiency of PDI. Thermal camera images of PDI/GGrS and the surface temperature change depending on the time are shown in Video S4.

Eq. S5 is used to determine the evaporation enthalpy for PDI/GGrS and the solar vapor conversion efficiency was calculated (by Eq. S4) as 96 %. The evaporation efficiency of the material is higher than GGrS (57 %) [33], which can be attributed to the ability of the supramolecule to absorb sunlight and convert it into thermal energy efficiently. It can also be concluded that PDI increases steam efficiency by acting as a barrier preventing heat loss at the surface.

3.7. Heat losses for the designed solar steam generation system

In the solar steam generation system, heat is lost in four different ways. These are evaporation, radiation, convection, and conduction [32]. The equations to calculate the heat loss are in the Supporting Information, and the results for PDI/GGrS are presented in Table S4. Radiation, convection, and conduction losses are low and dominant heat loss has been calculated 90 % for evaporation in PDI/GGrS, attributed to the fact that the supramolecule wraps the GGrS surface like a protective cover, minimizing thermal losses and converting solar into thermal energy with high efficiency [53]. Furthermore, PDI is also gradually immobilized on GGrS in addition to the gradient structure of GGrS, it is suggested that the gradient structure of these materials contributes to the prevention of thermal losses.

3.8. Solar thermal conversion efficiency of PDI/GGrS at different water contents

The evaporation rate and solar thermal conversion efficiency of PDI/GGrS in different water contents (pure water, acidic (pH: 2), and basic (pH: 12) solutions, the solutions containing separately 3.5 % NaCl, 100 mg/mL Cu^{2+}, and 1.0 g/L MO) were investigated, and the results were depicted in Fig. 5.a and Table S5. For PDI/GGrS, the % standard deviations of the evaporation rate and solar thermal conversion efficiency were calculated as 5.49 and 0.79, respectively. These values revealed that PDI/GGrS could work well in salty and wastewater, besides concentrated acid and alkaline solutions, promising for the application in the photothermal regeneration of clean water.

3.9. Desalination with PDI/GGrS

Two separate solutions containing 3.5 % NaCl and 0.1 % Na^+, K^+, Mg^{2+}, and Ca^{2+} ions were prepared for the desalination experiments to perform with PDI/GGrS. The ion contents before and after distillation with PDI/GGrS were determined by the ICP-MS, and the results were shown in Fig. 5.b and Table S6. Initially, 1275 ppm Na^+ was detected in the saltwater and 100 ppm Na^+ ions were detected after purification with PDI/GGrS. Table S6 demonstrates the ion content of the solution containing 0.1 % Na^+, K^+, Mg^{2+}, and Ca^{2+} ions before and after distillation. Desalination performance for PDI/GGrS was determined as 92 %. The high desalination activity of this material can be attributed to the easy electrostatic attraction between positively charged ions in saltwater and the negatively charged regions (functional groups such as hydroxyl, epoxy, carbonyl) in the porous sponge structure.

Furthermore, desalination experiments were carried out with Black

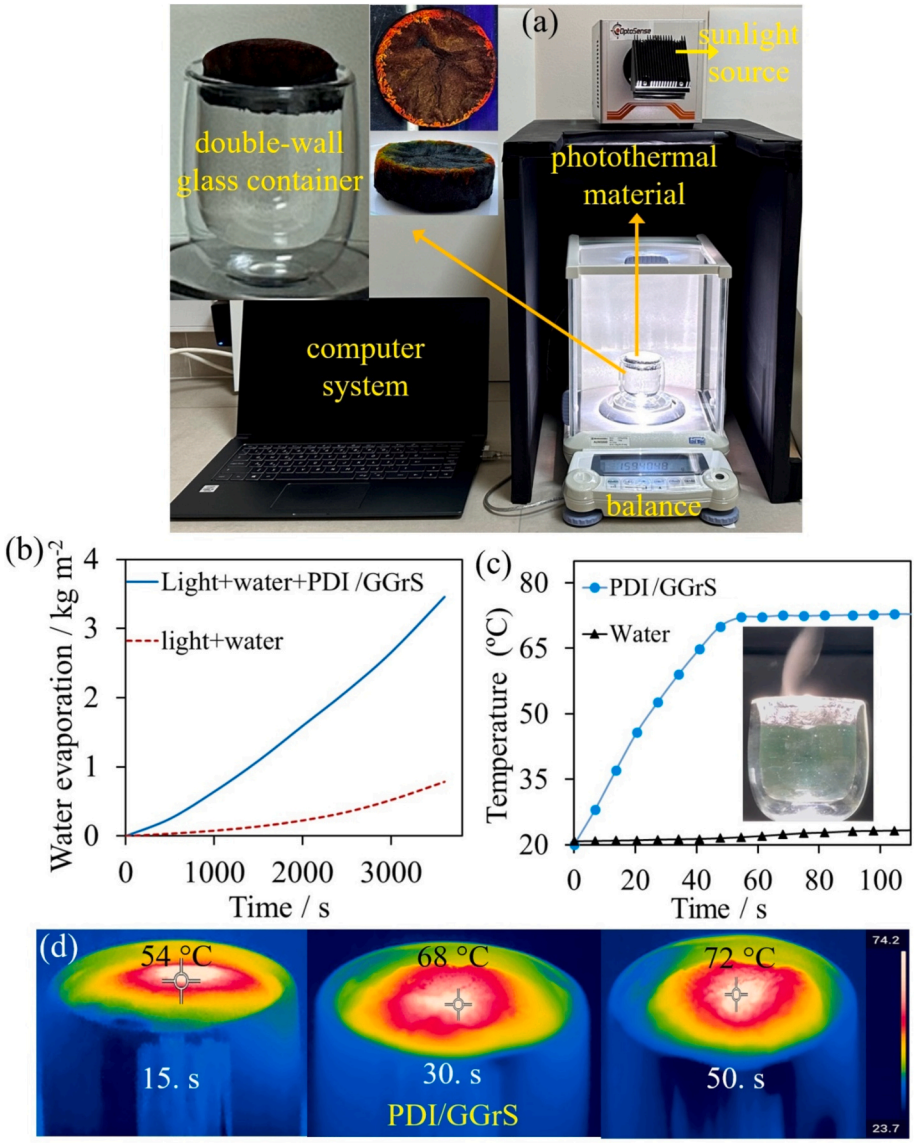

Fig. 4. (a) Water evaporation system with the PDI/GGrS (Inset: Photographs of PDI/GGrS under UV and daylight. (b) The amount of water evaporation with (blue line) and without (dashed red line) PDI/GGrS over time under sunlight. (c) The temperature during the 100 s irradiation of the water and PDI/GGrS. İnset: PDI/GGrS at the 40th second of the irradiation under sunlight. (d) Thermal camera images after different irradiation times for PDI/GGrS. (For interpretation of the references to colour in this figure legend, the reader is referred to the web version of this article.)

Sea and Mediterranean marine water. The results are presented as the solution conductivity in Table S7. The conductivity values of Mediterranean and Black Sea sea water, initially measured as 149 and 76 mS/cm, decreased to 36μS and 33μS after distillation with PDI/GGrS, respectively. Thus, PDI/GGrS achieved a desalination of about 99.6 % for real seawater, demonstrating a promising solar steam generator.

3.10. Purification of wastewater containing heavy metal with PDI/GGrS

Heavy metal ions in drinking water cause chronic poisoning by inactivating proteins and enzymes in the human body. For this reason, the removal of heavy metals in drinking water is of great importance. Solar thermal purification experiments of solutions containing 225 mg/mL Pb^{2+}, 100 mg/mL Cu^{2+}, 90 mg/mL Ni^{2+}, 75 ppm Cr^{3+}, and 150 mg/mL Zn^{2+} were carried out with PDI/GGrS (Fig. 5.c). From the results of the experiment (Table S8), the heavy metal removal performance for PDI/GGrS was determined as 97 %, thus, the purification of wastewater containing heavy metal ions is successfully achieved with PDI/GGrS.

3.11. Purification of acidic and alkaline solutions with PDI/GGrS

To test PDI/GGrS in the purification of concentrated acid and base solutions, solar thermal purification was carried out with acidic (pH: 2) and alkaline (pH: 12) solutions. The acidic and alkaline solutions reached neutral pH after solar thermal purification with PDI/GGrS (Fig. 5.d). Removal in the acidic solution is supposed to occur with the electrostatic attraction between H_3O^+ ions and the negatively charged functional groups of graphene-based materials. The purification in the alkaline solution can be assigned to the adsorption of OH^- ions to the pores in the sponge structure. The results revealed that PDI/GGrS is an effective photothermal material for the purification of the acidic/basic solutions.

3.12. Purification of wastewater containing dye with PDI/GGrS

The solar purification performance of PDI/GGrS was investigated in dye solutions containing 1.0 g/L MO and methylene blue (MB). These dyes have a charged and a regular π conjugated system (Fig. S7a and b).

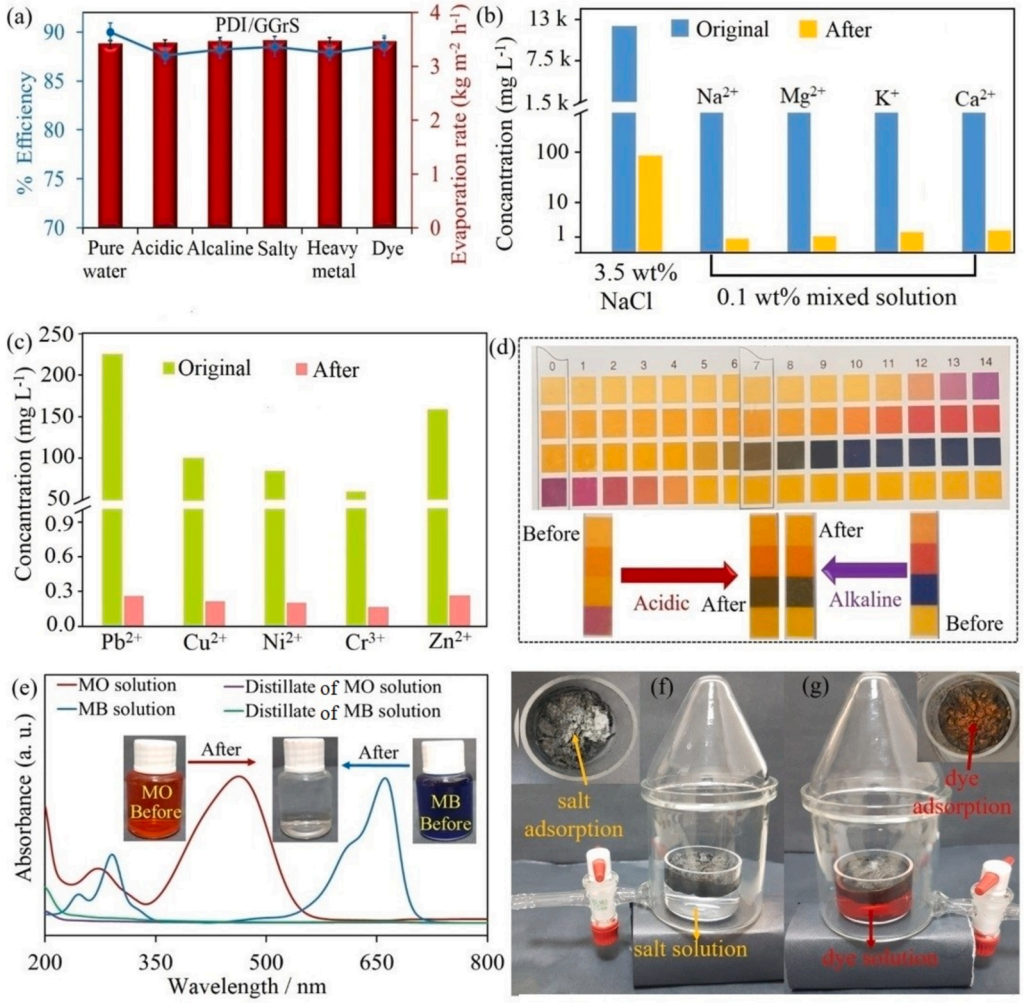

Fig. 5. (a) Water evaporation rate and solar thermal conversion efficiency of PDI/GGrS in different solutions after 1 h under 1 sunlight. After distillation with PDI/GGrS, the changes in ion amounts in (b) 3.5 % NaCl solution and solution containing 0.1 % Na^{+}, K^{+}, Mg^{+2}, and Ca^{+2} ions (k:1000), (c) 225 mg/mL Pb^{+2}, 100 mg/mL Cu^{+2}, 90 mg/mL Ni^{+2}, 75 ppm Cr^{+3}, 150 mg/mL Zn^{+2}. (d) images of pH values before and after solar thermal purification of the acidic (pH: 2) and alkaline (pH: 12) solutions with PDI/GGrS. (e) UV–visible absorption spectra and the photographs of MO and MB dye solutions before and after solar purification. The photographs of the distillation system for solar purification of (f) salty water and (g) MO solution. Inset: The photographs of PDI/GGrS after distillation.

The distillate of the solutions after under 10 sun irradiation for 2 h was examined by UV–visible absorption spectroscopy (Fig. 5.e). After solar purification with PDI/GGrS, the UV–visible absorption spectrum of the distillates was very similar to that of pure water. In addition, photographs of both dye solutions before and after distillation displayed clear purification of dyes. The dye purification was acquired by adsorption to sponge surfaces through both π-π interactions and electrostatic interactions between dyes and graphene [54]. Further, photographs of the PDI/GGrS after distillation (Fig. 5.f and g) show that salt and MO dye accumulated on the material surface. Distillation of MO solution with PDI/GGrS is presented in the Video S5, which indicates that PDI/GGrS is a promising material for solar steam generation in the purification of dye-containing wastewater.

3.13. Antibacterial properties of PDI/GGrS

The antibacterial properties of PDI/GGrS was tested using Gram-negative species of *E. coli*. The results of bacterial counts performed for 24 h are presented in the Fig. S8. Since no material existed in the control group, bacteria continued to multiply. On the other hand, in the presence of PDI/GGrS, the amount of bacteria decreased by 25 %, which is attributed to the partially antimicrobial effect of PDI.

3.14. Photothermal properties and stability of PDI/GGrS under daylight

Fig. 6.a depicts the evaporation rate for PDI/GGrS depending on the solar energy intensity under daylight. The evaporation rate of the material increase proportionally as the solar energy intensity increases, indicating that PDI/GGrS is sensitive to the solar energy intensity. PDI/GGrS was used as photothermal material in the open-air system shown in Fig. S9. The amount of water collected against the solar flux during one day was recorded in Fig. 6.a. Experiments were carried out in Erzurum-Türkiye (average temperature: 25 °C; humidity: 58 %, sunrise 04:50, sunset 19:20) in July. The solar flux and the amount of distilled water increased with sunrise and decreased near sunset (Fig. 6.a). The results under daylight were close to the evaporation amounts obtained under 1.0 kW cm^{-2} sunlight under laboratory conditions, indicating that our photothermal material can also be used in solar steam generation applications under daylight.

3.15. Long-term stability of PDI/GGrS

To test the long-term stability of PDI/GGrS, the solar evaporation was repeated for 25 cycles using the same material. In each cycle, the water-wetted and swollen material was taken out of the system, and the adsorbed water was removed by mass pressure. The materials were

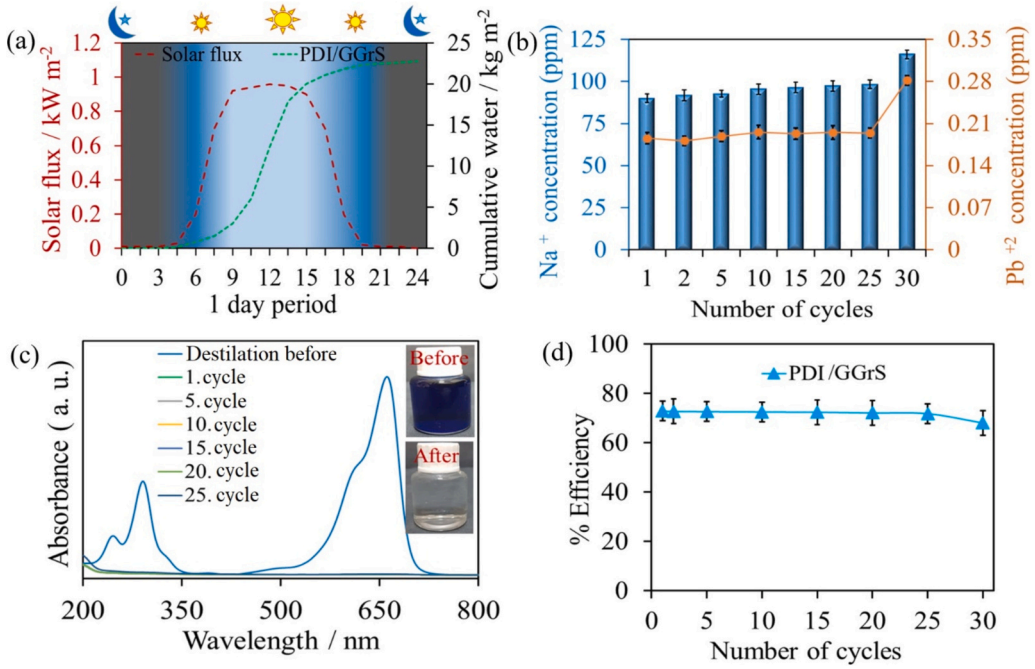

Fig. 6. (a) The amount of distilled water depending on the solar flux during the day. Concentrations of distillates obtained after 30 consecutive uses of PDI/GGrS in the distillation of solutions containing (b) 900 ppm Na^+ and and 225 ppm Pb^{2+}. (c) UV–visible absorption spectra before distillation and after 1, 5, 10, 15, 20, and 25 cycles of solar purification with PDI/GGrS. Inset: The photographs of MB dye solution before and after 25. cycle of solar purification with PDI/GGrS. (d) The solar thermal conversion effiency of PDI/GGrS after 30 cycles of utility.

dried at 60 °C for 20 min and reused in the next cycle (Fig. S10). Ion contents in the water at the end of each cycle were detected by the ICP-MS, and dye content by UV–visible absorption spectroscopy. Compared to the solution containing 900 ppm Na^+ at the beginning, it was determined as 95 and 100 ppm Na^+ after the 1st and 25th cycle of PDI/GGrS in the solar steam generator system, respectively, which acquired an 88 % removal performance after 25 cycle (Fig. 6.b). In a similar study, it was observed that initially containing 225 ppm Pb^{2+} of a solution was reduced to 0.18 and 1.70 ppm Pb^{2+} concentration, respectively, after the 1st and 25th cycle distillations with PDI/GGrS, demonstrating a 98 % purification efficiency of the material (Fig. 6.b). After the 25th cycle, the removal performance of the material decreased by more than 30 % compared to the first cycle, which is due to structural deformations of graphene structures as a result of wetting and drying.

Another study was carried out by using PDI/GGrS with high photothermal activity for 25 consecutive cycles in the distillation of a solution containing MB dye at a concentration of 1.0 g/L. Fig. 6.c demonstrates that the UV–visible absorption spectra of the distillates obtained after the 1st and 25th cycles are almost the same. These results indicate that the material exhibits high dye removal performance even with consecutive usage.

In Fig. 6.d, as the number of cycles increased, there was no significant change in evaporation efficiency until the 25th cycle. Even after the 30th cycle, the vapor generation efficiency was reduced by only 11 %. The photographs in Fig. 7.a show that the material is structurally stable. SEM images (Fig. 7.b) and EDX spectrum (Fig. S11) of PDI/GGrS were recorded to investigate why the photothermal performance decreased after the 25th cycle. No significant change in the morphological

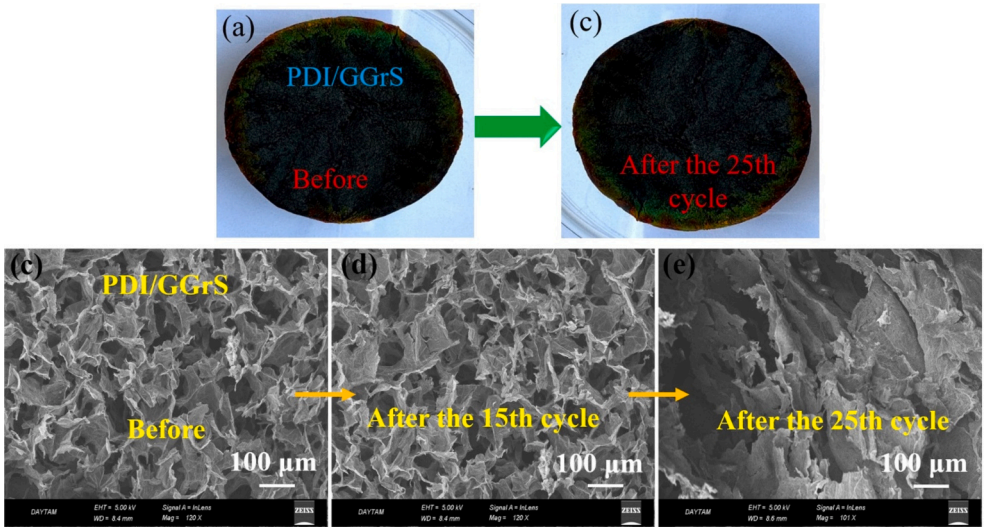

Fig. 7. Photographs (a,b) and SEM images (b,c,d) of PDI/GGrS before and after the 25th cycle used as a photothermal material.

structure of the material was observed after the 15th cycle. However, after the 25th cycle, the graphene layers underwent deformation due to successive wetting, pressing, and drying processes (Fig. S10). This deformation caused the pores to shrink and, accordingly, the amount of water transported per unit time and the vapor generation performance to decrease. EDX spectra of PDI/GGrS showed no obvious change in elemental atomic ratios with the increasing number of cycles (Fig. S11). The decrease (11 %) in photothermal efficiency after the 30th cycle was not due to the structural change of PDI/GGrS but to the physical collapse of the 3D graphene sponge structure.

3.16. The reproducibility of PDI/GGrS

Four PDI/GGrSs were prepared at different times using the same method, and each of them was used as the photothermal material for solar steam generation. PDI/GGrSs showed evaporation rates with RSD of % 1.9. (Fig. S1), demonstrating that materials with the same structural and chemical properties can be obtained by using the proposed preparation procedure.

Compared to other graphene-based materials, such as Janus VA-MXA (1.46 kg/m^2h, 87 %) [55], 3DG (1.2 kg/m^2h, 80 %) [32], GGSM (1.79 kg/m^2h, 57 %) [33], and VA-GSM (1.62 kg/m^2h, 86.5 %) [18], PDI/GGrS achieved a high steam generation performance of 3.5 kg/m^2h under 1 sunlight and a superior solar thermal conversion efficiency of up to 90 %, thanks to the high sunlight adsorption and excellent photothermal property of PDI molecules.

In addition, the SSG performance of the materials with Janus structure in the literature were compared with PDI/GGrS in Table S9. Especially the thermal efficiencies and evaporation rates were relatively low due to the thermal losses that occur because of two different materials in the Janus structure. On the other hand, PDI/GGrS minimizes heat losses thanks to a whole material (not Janus) and achieves higher evaporation performance due to PDI and GGrS having high photothermal activity.

Desalination methods, such as distillation, reverse osmosis, and electrodialysis face cost, effectiveness, and scalability hurdles. However, photothermal distillation is a technology that uses a large amount of solar energy to obtain clean water by evaporation, with a wide range of applications in fields such as water treatment, seawater desalination, and wastewater remediation. This study offers a new material for a cost-effective solar water purification system with a high evaporation rate and thermal efficiency.

PDI/GGrS, which is used in salt, heavy metal, dye, and acid-base removal, adsorbs a large amount of ions into its pores. After purification and desalination, PDI/GGrS can have high performance in flexible supercapacitor circuits. Thus, it is of great importance that the same material will be used in both solar steam generator systems and supercapacitor circuit designs, which are at the forefront in terms of environment and sustainability. Our studies are continuing with PDI/GGrS, which was first used in desalination-purification in a solar steam generator system, and then in the design of a flexible supercapacitor circuit.

4. Conclusion

In summary, we have reported the photothermal activity of PDIs with an efficient graphene-based material in the solar steam generator system for the first time. PDI/GGrS possesses a floating 3D graphene sponge facilitating water transport, high light absorption with PDI, and excellent stability in strict conditions with highly efficient solar thermal conversion for the generation of clean water from seawater, wastewater, and even acidic/alkali solutions. As a result, our system achieved a superior high efficiency of up to 90 % and a water evaporation rate of 3.5 kg h^{-1} m^{-2} under 1 sun. Moreover, stable and repeated solar purification tests were performed with PDI/GGrS both in the laboratory and an outdoor environment proving that combining supramolecules with a 3D graphene sponge can greatly help in enhancing solar steam generation. This design concept provides a promising route for solar-driven water desalination and purification.

Supplementary data to this article can be found online at https://doi.org/10.1016/j.desal.2024.118237.

Declaration of competing interest

The authors declare that they have no known competing financial interests or personal relationships that could have appeared to influence the work reported in this paper.

Acknowledgments

This study was supported by the Scientific and Technological Research Council of Turkey (TUBITAK) under Project no. 121M347 and Atatürk University (Project: BAP-FDA-2022-10828). We thank Dr. Songül BAYRAK and Dr. Mustafa Özkan BALTACI for their contributions to antibacterial studies.

Data availability

The authors do not have permission to share data.

References

[1] H. Piao, J. Zhao, Y. Tang, R. Zhang, S. Zhang, Q. Huang, S. Zuo, Y. Liu, C. Xiao, S. Liu, On-demand switchable superamphiphilic nanofiber membrane reinforced by PET braided tube for efficient wastewater purification and photocatalytic regeneration, Appl. Catal. B Environ. 341 (2024), https://doi.org/10.1016/j.apcatb.2023.123300.

[2] J. Zhao, Q. Huang, S. Gao, H. Piao, Q. Quan, C. Xiao, In situ photo-thermal conversion nanofiber membrane consisting of hydrophilic PAN layer and hydrophobic PVDF-ATO layer for improving solar-thermal membrane distillation, J. Membr. Sci. 635 (2021), https://doi.org/10.1016/j.memsci.2021.119500.

[3] Q. Hu, M.K. Albolkany, C. Liu, T. Zhang, S. Cui, F. Ye, B. Liu, Photothermal graphite phase carbon nitride membrane intercalated with polyoxovanadate for efficient solar steam generation, Desalination 583 (2024) 117650, https://doi.org/10.1016/j.desal.2024.117650.

[4] K. Li, X. Liu, T. Zheng, D. Jiang, Z. Zhou, C. Liu, X. Zhang, Y. Zhang, D. Losic, Tuning MnO2 to FeOOH replicas with bio-template 3D morphology as electrodes for high performance asymmetric supercapacitors, Chem. Eng. J. 370 (2019) 136–147, https://doi.org/10.1016/j.cej.2019.03.190.

[5] L. Zhang, B. Tang, J. Wu, R. Li, P. Wang, Hydrophobic light-to-heat conversion membranes with self-healing ability for interfacial solar heating, Adv. Mater. 27 (2015) 4889–4894, https://doi.org/10.1002/adma.201502362.

[6] W. Zhang, G. Zhang, Q. Ji, H. Liu, R. Liu, J. Qu, Capillary-flow-optimized heat localization induced by an air-enclosed three-dimensional hierarchical network for elevated solar evaporation, ACS Appl. Mater. Interfaces 11 (2019) 9974–9983, https://doi.org/10.1021/acsami.8b21800.

[7] Y. Wei, W. Li, S. Zhang, J. Yu, Y. Tang, J. Wu, S. Yu, Laser-induced porous graphene/CuO composite for efficient interfacial solar steam generation, Adv. Funct. Mater. 34 (2024) 1–10, https://doi.org/10.1002/adfm.202401149.

[8] L. Noureen, Q. Wang, P.M. Ismail, M. Alomar, N. Arshad, M.S. Irshad, Q. Xu, X. Wang, Multifunctional aerogel with antibiofouling properties for efficient solar steam generation and seawater desalination, Nano Today 54 (2024) 102130, https://doi.org/10.1016/j.nantod.2023.102130.

[9] K.K. Liu, Q. Jiang, S. Tadepalli, R. Raliya, P. Biswas, R.R. Naik, S. Singamaneni, Wood-graphene oxide composite for highly efficient solar steam generation and desalination, ACS Appl. Mater. Interfaces 9 (2017) 7675–7681, https://doi.org/10.1021/acsami.7b01307.

[10] Y. Fu, G. Wang, T. Mei, J. Li, J. Wang, X. Wang, Accessible graphene aerogel for efficiently harvesting solar energy, ACS Sustain. Chem. Eng. 5 (2017) 4665–4671, https://doi.org/10.1021/acssuschemeng.6b03207.

[11] J. Bang, I.K. Moon, J. Oh, Three-dimensional multimodal porous graphene-carbonized wood for highly efficient solar steam generation, Sustain. Energy Technol. Assess. 57 (2023) 103199, https://doi.org/10.1016/j.seta.2023.103199.

[12] A. Zhang, K. Wang, M.J. Nine, M. Cao, H. Zong, Z. Liu, H. Guo, J. Liu, D. Losic, Natural high-porous diatomaceous-earth based self-floating aerogel for efficient solar steam power generation, green, Energy Environ. 9 (2024) 378–389, https://doi.org/10.1016/j.gee.2022.08.001.

[13] Q.F. Guan, Z.M. Han, Z.C. Ling, H. Bin Yang, S.H. Yu, Sustainable wood-based hierarchical solar steam generator: a biomimetic design with reduced vaporization enthalpy of water, Nano Lett. 20 (2020) 5699–5704, https://doi.org/10.1021/acs.nanolett.0c01088.

[14] L. Yang, G. Chen, N. Zhang, Y. Xu, X. Xu, Sustainable biochar-based solar absorbers for high-performance solar-driven steam generation and water purification, ACS Sustain. Chem. Eng. 7 (2019) 19311–19320, https://doi.org/10.1021/acssuschemeng.9b06169.

[15] H. Xu, Y. Lu, F. Jiang, J. Zhang, Y. Ge, Z. Li, 3D porous N-doped lignosulfonate/graphene oxide aerogel for efficient solar steam generation and desalination, Int. J. Biol. Macromol. 233 (2023) 123469, https://doi.org/10.1016/j.ijbiomac.2023.123469.
[16] M. Xie, P. Zhang, Y. Cao, Y. Yan, Z. Wang, C. Jin, A three-dimensional antifungal wooden cone evaporator for highly efficient solar steam generation, Npj Clean Water 6 (2023) 1–9, https://doi.org/10.1038/s41545-023-00231-3.
[17] A. Ghaffar, M. Usman, M.U. Khan, M. Hassan, Simultaneous solar steam and electricity generation from biochar based photothermal membranes, J. Clean. Prod. 446 (2024) 141374, https://doi.org/10.1016/j.jclepro.2024.141374.
[18] P. Zhang, J. Li, L. Lv, Y. Zhao, L. Qu, Vertically aligned graphene sheets membrane for highly efficient solar thermal generation of clean water, ACS Nano 11 (2017) 5087–5093, https://doi.org/10.1021/acsnano.7b01965.
[19] M. Toyoda, M. Inagaki, Carbon materials for solar steam-generation, Carbon N. Y. 214 (2023) 118373, https://doi.org/10.1016/j.carbon.2023.118373.
[20] A. Guo, X. Ming, Y. Fu, G. Wang, X. Wang, Fiber-based, double-sided, reduced graphene oxide films for efficient solar vapor generation, ACS Appl. Mater. Interfaces 9 (2017) 29958–29964, https://doi.org/10.1021/acsami.7b07759.
[21] J. Yang, Y. Chen, X. Jia, Y. Li, S. Wang, H. Song, Wood-based solar Interface evaporation device with self-desalting and high antibacterial activity for efficient solar steam generation, ACS Appl. Mater. Interfaces 12 (2020) 47029–47037, https://doi.org/10.1021/acsami.0c14068.
[22] X. Yin, Y. Zhang, Q. Guo, X. Cai, J. Xiao, Z. Ding, J. Yang, Macroporous double-network hydrogel for high-efficiency solar steam generation under 1 sun illumination, ACS Appl. Mater. Interfaces 10 (2018) 10998–11007, https://doi.org/10.1021/acsami.8b01629.
[23] Z. Guo, G. Wang, X. Ming, T. Mei, J. Wang, J. Li, J. Qian, X. Wang, PEGylated self-growth MoS2 on a cotton cloth substrate for high-efficiency solar energy utilization, ACS Appl. Mater. Interfaces 10 (2018) 24583–24589, https://doi.org/10.1021/acsami.8b08019.
[24] P. Sun, W. Wang, W. Zhang, S. Zhang, J. Gu, L. Yang, D. Pantelić, B. Jelenković, D. Zhang, 3D interconnected gyroid au-cus materials for efficient solar steam generation, ACS Appl. Mater. Interfaces 12 (2020) 34837–34847, https://doi.org/10.1021/acsami.0c06701.
[25] T. Chen, Z. Wu, Z. Liu, J.T. Aladejana, X. (Alice) Wang, M. Niu, Q. Wei, Y. Xie, Hierarchical porous aluminophosphate-treated wood for high-efficiency solar steam generation, ACS Appl. Mater. Interfaces 12 (2020) 19511–19518. doi: https://doi.org/10.1021/acsami.0c01815.
[26] J. Chen, B. Li, G. Hu, R. Aleisa, S. Lei, F. Yang, D. Liu, F. Lyu, M. Wang, X. Ge, F. Qian, Q. Zhang, Y. Yin, Integrated evaporator for efficient solar-driven interfacial steam generation, Nano Lett. 20 (2020) 6051–6058, https://doi.org/10.1021/acs.nanolett.0c01999.
[27] H. Li, H. Li, H. Li, H. Wen, J. Li, J. Li, J. Huang, J. Huang, J. Huang, D. Wang, B. Z. Tang, Doping AIE photothermal molecule into all-fiber aerogel with self-pumping water function for efficiency solar steam generation, ACS Appl. Mater. Interfaces 12 (2020) 26033–26040, https://doi.org/10.1021/acsami.0c06181.
[28] H. Yang, Z. Li, B. Lu, J. Gao, X. Jin, G. Sun, G. Zhang, P. Zhang, L. Qu, Reconstruction of inherent graphene oxide liquid crystals for large-scale fabrication of structure-intact graphene aerogel bulk toward practical applications, ACS Nano 12 (2018) 11407–11416, https://doi.org/10.1021/acsnano.8b06380.
[29] K.S. Novoselov, D. Jiang, F. Schedin, T.J. Booth, V.V. Khotkevich, S.V. Morozov, A. K. Geim, Novoselov_Geim_PNAS_2005_2D atomic crystals.pdf 102 (2005) 10451–10453.
[30] K. Dağcl Klranşan, E. Topçu, Conducting polymer-reduced graphene oxide sponge electrode for electrochemical detection based on DNA hybridization, ACS Appl. Nano Mater. 3 (2020) 5449–5462, https://doi.org/10.1021/acsanm.0c00782.
[31] E. Erçarıkcı, Z. Aksu, E. Topçu, K. Dağcı Kıranşan, Design of metal phosphite decorated sponge materials for high-performance flexible battery-type supercapacitors, Int. J. Energy Res. (2022) 1–18, https://doi.org/10.1002/er.8653.
[32] Y. Yang, R. Zhao, T. Zhang, K. Zhao, P. Xiao, Y. Ma, P.M. Ajayan, G. Shi, Y. Chen, Graphene-based standalone solar energy converter for water desalination and purification, ACS Nano 12 (2018) 829–835, https://doi.org/10.1021/acsnano.7b08196.
[33] E. Erçarıkcı, E. Topçu, Z. Kudaş, Z. Aksu, M. Alanyalıoğlu, K. Dağcı Kıranşan, An effective material for solar steam generation applications: gradient graphene sponge, Mater. Today Sustain. 26 (2024) 1–11, https://doi.org/10.1016/j.mtsust.2024.100701.
[34] L. Zhao, Y. Liu, R. Xing, X. Yan, Supramolecular photothermal effects: a promising mechanism for efficient thermal conversion, Angew. Chem. Int. Ed. 59 (2020) 3793–3801, https://doi.org/10.1002/anie.201909825.
[35] A. Harriman, Ö.A. Bozdemir, D.D. Gultekin, Triplet distribution in a symmetrical zinc (II) porphyrin-BODIPY pentameric array, J. Phys. Chem. A 124 (2020) 10736–10747, https://doi.org/10.1021/acs.jpca.0c09243.
[36] N. Micali, P. Mineo, F. Vento, A. Nicosia, V. Villari, Supramolecular structures formed in water by graphene oxide and nonionic PEGylated porphyrin: interaction mechanisms and fluorescence quenching effects, J. Phys. Chem. C 123 (2019) 25977–25984, https://doi.org/10.1021/acs.jpcc.9b06800.
[37] V.A. Povedailo, B.V. Ronishenko, V.I. Stepuro, D.A. Tsybulsky, V.V. Shmanai, D. L. Yakovlev, Fluorescence quenching of dyes by graphene oxide, J. Appl. Spectrosc. 85 (2018) 605–610, https://doi.org/10.1007/s10812-018-0693-6.
[38] Y. Jinjin Wang, W. Song, Z. Chen, X. Ma, J. Wang, H. Zhang Han, Theoretical investigation on the structural and spectroscopic properties of "cross" [anthraquinone-diamine/diimine-Pt] complexes, Russ. J. Phys. Chem. A 93 (2019) 2570–2574, https://doi.org/10.1134/S0036024419120112.
[39] Y. Jiao, K. Liu, G. Wang, Y. Wang, X. Zhang, Supramolecular free radicals: near-infrared organic materials with enhanced photothermal conversion, Chem. Sci. 6 (2015) 3975–3980, https://doi.org/10.1039/c5sc01167a.
[40] W.S. Hummers, R.E. Offeman, Preparation of graphitic oxide, J. Am. Chem. Soc. 80 (1958) 1339, https://doi.org/10.1021/ja01539a017.
[41] Y.S. Ma, C.H. Wang, Y.J. Zhao, Y. Yu, C.X. Han, X.J. Qiu, Z. Shi, Perylene diimide dyes aggregates: optical properties and packing behavior in solution and solid state, Supramol. Chem. 19 (2007) 141–149, https://doi.org/10.1080/10610270600902324.
[42] F. Zhang, Y. Ma, Y. Chi, H. Yu, Y. Li, T. Jiang, X. Wei, J. Shi, Self-assembly, optical and electrical properties of perylene diimide dyes bearing unsymmetrical substituents at bay position, Sci. Rep. 8 (2018) 1–11, https://doi.org/10.1038/s41598-018-26502-5.
[43] A. Marjani, A.T. Nakhjiri, M. Adimi, H.F. Jirandehi, S. Shirazian, Effect of graphene oxide on modifying polyethersulfone membrane performance and its application in wastewater treatment, Sci. Rep. 10 (2020) 1–11, https://doi.org/10.1038/s41598-020-58472-y.
[44] X. Wang, T. Zeng, M. Nourrein, B.H. Lai, K. Shen, C.L. Wang, B. Sun, M. Zhu, Concentration-dependent self-assembly structures of an amphiphilic perylene diimide with tri(ethylene glycol) substituents at bay positions, RSC Adv. 7 (2017) 26074–26081, https://doi.org/10.1039/c7ra04296e.
[45] M. Bera, P. Chandravati, P.K. Gupta, Maji, facile one-pot synthesis of graphene oxide by sonication assisted mechanochemical approach and its surface chemistry, J. Nanosci. Nanotechnol. 18 (2017) 902–912, https://doi.org/10.1166/jnn.2018.14306.
[46] D. Demirci Gültekin, Aromatic stacking and the self-assembly of perylene monoimide diester homodimers, J. Photochem. Photobiol. A Chem. 426 (2022) 113769, https://doi.org/10.1016/j.jphotochem.2022.113769.
[47] G. Montagnac, H. Cardon, I. Daniel, B. Reynard, Structural changes in perylene from UV Raman spectroscopy up to 1 GPa, J. Raman Spectrosc. 47 (2016) 720–725, https://doi.org/10.1002/jrs.4890.
[48] M. Angelella, C. Wang, M.J. Tauber, Resonance Raman spectra of a perylene bis (dicarboximide) chromophore in ground and lowest triplet states, J. Phys. Chem. A 117 (2013) 9196–9204, https://doi.org/10.1021/jp407879k.
[49] Z. Luo, Y. Luo, J. Li, K. Liu, H. Fu, Y. Ma, J. Yao, Stabilizing single-molecular Raman spectrum of a nonbonding molecule on Ag nanoparticles, Chem. Commun. (2009) 1342–1344, https://doi.org/10.1039/b819402e.
[50] X. Yang, X. Niu, Z. Mo, R. Guo, N. Liu, P. Zhao, Z. Liu, Perylene-functionalized graphene sheets modified with chitosan for voltammetric discrimination of tryptophan enantiomers, Microchim. Acta 186 (2019), https://doi.org/10.1007/s00604-019-3442-5.
[51] Y. Xu, J. Wang, F. Yu, Z. Guo, H. Cheng, J. Yin, L. Yan, X. Wang, Flexible and efficient solar thermal generators based on polypyrrole coated natural latex foam for multimedia purification, ACS Sustain. Chem. Eng. 8 (2020) 12053–12062, https://doi.org/10.1021/acssuschemeng.0c03164.
[52] Q. Zou, M. Abbas, L. Zhao, S. Li, G. Shen, X. Yan, Biological photothermal nanodots based on self-assembly of peptide-porphyrin conjugates for antitumor therapy, J. Am. Chem. Soc. 139 (2017) 1921–1927, https://doi.org/10.1021/jacs.6b11382.
[53] Z. Liu, H. Song, D. Ji, C. Li, A. Cheney, Y. Liu, N. Zhang, X. Zeng, B. Chen, J. Gao, Y. Li, X. Liu, D. Aga, S. Jiang, Z. Yu, Q. Gan, Extremely cost-effective and efficient solar vapor generation under nonconcentrated illumination using thermally isolated black paper, Global Chall. 1 (2017) 1–10, https://doi.org/10.1002/gch2.201600003.
[54] E. Erçarikci, K. Dağci, E. Topçu, M. Alanyalioğlu, Electrochemical preparation of poly(methylene blue)/graphene nanocomposite thin films, Mater. Res. Bull. 55 (2014) 95–101, https://doi.org/10.1016/j.materresbull.2014.04.006.
[55] Q. Zhang, G. Yi, Z. Fu, H. Yu, S. Chen, X. Quan, Vertically aligned Janus MXene-based aerogels for solar desalination with high efficiency and salt resistance, ACS Nano 13 (2019) 13196–13207, https://doi.org/10.1021/acsnano.9b06180.